The phosphorescent properties of heteroleptic Ir (III) complexes: uncovearing their emissive species

Prashant Kumar[a], Manuel Pérez-Escribano[a], Davita M. E. van Raamsdonk[a], Daniel Escudero[a]*

[a]Department of Chemistry, KU Leuven, Celestijnenlaan 200F, B-3001 Leuven, Belgium

* **Corresponding author**

Email address: daniel.escudero@kuleuven.be – Tel. +32 16 19 33 53

KEYWORDS: Phosphorescence, Ir(III) complexes, DLPNO-CCSD(T), OLEDs, Excited states, vibronically resolved emission spectra and phosphorescent rates

ABSTRACT

In this contribution we assess the computational machinery to calculate the phosphorescence properties of a large pool of heteroleptic $[Ir(C\char`\^N)_2(N\char`\^N)]^+$ complexes (where $N\char`\^N$ is an ancillary ligand and $C\char`\^N$ is a cyclometalating ligand) including their phosphorescent rates and their emission spectra. Efficient computational protocols are next proposed. Specifically, different flavors of DFT functionals were benchmarked against DLPNO-CCSD(T) for the phosphorescence energies. Transition density matrix and decomposition analysis of the emitting triplet excited state enables to categorize the studied complexes into different cases, from e.g., predominant triplet ligand-centered (^{3}LC) character to predominant charge-transfer (^{3}CT) character, either of metal-to-ligand charge transfer (^{3}MLCT), ligand-to-ligand charge transfer (^{3}LLCT) or a combination of the two. We have also calculated the vibronically resolved phosphorescent spectra and rates. Ir (III) complexes with predominant ^{3}CT character are characterized by less vibronically-resolved bands as compared to those with predominant ^{3}LC character. Furthermore, some of the complexes are characterized by close-lying triplet excited states, so that the calculation of their phosphorescence properties poses additional challenges. In these scenarios, it is necessary to perform geometry optimizations of higher-lying triplet excited states (i.e., T_n). We demonstrate that in the latter scenarios all the close-lying triplet species must be considered to recover the shape of the experimental emission spectra. The global analysis of computed emission energies, shape of the computed emission spectra, computed rates, etc. enable us to unambiguously pinpoint for the first time the triplet states involved in the emission process and to provide a general classification of Ir (III) complexes with regards to their phosphorescent properties.

1. INTRODUCTION

In the last decades transition metal complexes (TMCs) have attracted significant interest from industry as well as academia because of their exceptional room-temperature phosphorescent properties.[1,2] Among TMCs with optimal optoelectronic properties, those of d^6 transition metal atoms, especially Ir(III), have found tremendous interest in the community for organic light emitting diodes (OLEDs),[3–7] optical sensors,[8,9] photocatalysts,[10,11] light emitting electrochemical cells (LECs),[12,13] bioimaging,[14] photodynamic therapy[15,16] and dye-sensitized solar cells.[17] Ir(III) complexes possess tailored chemical, physical and photophysical properties for these applications including high photostability, limited access to non-emissive states, long-lived excited state lifetimes and tunable emission color through ligand alteration in the complex. In this work, we focus on pseudo-octahedral heteroleptic *fac*-[Ir(C^N)^2(N^N)]$^+$ complexes (where C^N is the cyclometalating ligand and N^N is the ancillary ligand, see Figure 1) because of their modular framework and abundant experimental data availability.[18,19] In total, we have chosen a set of 30 Ir(III) complexes with structurally diverse chemical motifs in both cyclometalating and ancillary ligands (see Table S8 in the SI). We chose different cyclometalating ligands including 2-phenylpyridine (ppy), 1-phenylpyrazole (phpz), 2-phenylbenzoxazole (PBO) and 2-phenylbenzothiazole (pbt) and different ancillary ligands including 2,2′-bipyridine (bpy) and 1,10-phenanthroline (phen).
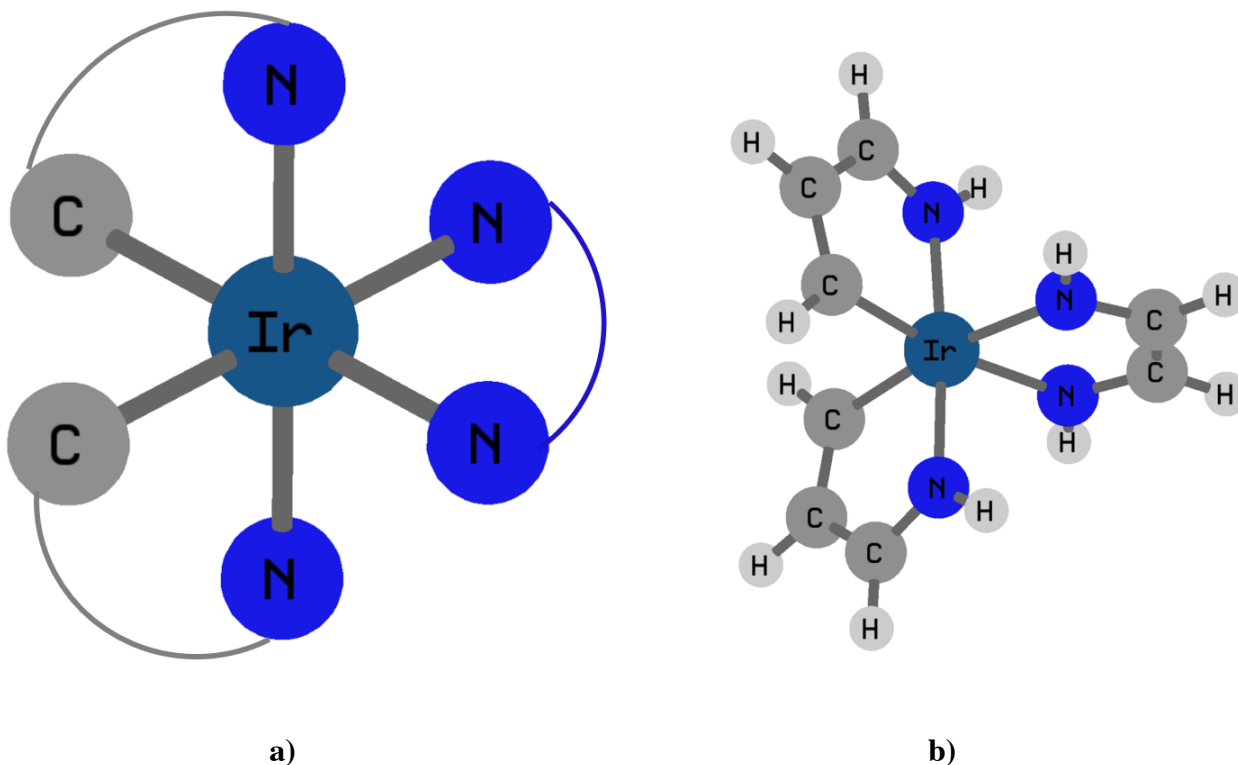
Figure 1. a) Heteroleptic [Ir(C^N)2(N^N)]+ complexes under investigation (N^N is the ancillary ligand and C^N is the cyclometalating ligand. b) Ad-hoc complex used for benchmarking purposes.

Femtosecond transient-absorption experiments reveal that after excitation to the manifold of singlet excited states in Ir(III) complexes ultrafast intersystem crossing (ISC) occurs in less than 100 fs, resulting in the formation of triplet excited states with near-unity quantum yield. For these complexes nonradiative channels involving triplet metal-centred excited states (^{3}MC) are often involved in the quenching of their photoluminescence lifetimes and efficiencies.[5,20] Their phosphorescence properties often arises from their lowest triplet excited state, i.e. the Kasha state, but other possible emitting scenarios (e.g., dual phosphorescence) have also been reported for these complexes.[21–23] The intricate emissive scenarios found in these complexes poses significant challenges for the modelling of their phosphorescent properties. We note that

these situations are not only found for Ir(III) complexes, but also for square-planar Pt(II) complexes, as recently shown by some of us.[24] When modeling phosphorescence the focus is often set on accurately calculating their phosphorescence energies only. Towards this end, ΔSCF and/or linear response methods are used most frequently in the community. These methods rely on optimizing the geometry of the lowest triplet excited state (T_1) and subsequently use this geometry to calculate the emission energy. Often, less efforts are devoted to the modeling of other relevant aspects, such as e.g., the nature and character of the emitting state, the phosphorescence rate and the shape of the phosphorescence spectrum.[25–27] Therefore, in this contribution we go beyond these initial works by providing a solid computational protocol to model all relevant aspects of phosphorescence of Ir(III) complexes.

To obtain accurate energies, within the hierarchy of coupled cluster methods, canonical coupled cluster method with singlet, doublet, and perturbative triplet excitations, i.e., CCSD(T) is the gold standard quantum chemical method. However, because of its high computational cost, its applicability is limited to small-size molecular systems.[28] Recent progresses to reduce the high-order scaling of CCSD(T) have led to the development of the Domain-Based Local Pair Natural Orbital Coupled Cluster theory with single, double, and perturbative triple excitations method, i.e., DLPNO-CCSD(T), which enables to treat medium-to-large size molecular systems.[29–32] In this contribution, the DLPNO-CCSD(T) energies correspond to our best theoretical estimates. We have validated the DLPNO-CCSD(T) results against canonical CCSD(T) for a small ad-hoc Ir complex (see complex in Figure 1b). The focus is set on assessing the effect of using different guesses (i.e., either HF-based or DFT-based). Next, we used our DLPNO-CCSD(T) theoretical best estimates to assess the performance of DFT-based approaches for complexes **1**-**30**. Further, to get insights into the nature and character of the

emitting state, we have performed Transition density matrix and decomposition analysis of the TD-DFT and TDA-DFT results, using the THEODORE software package.[33,34]

Finally, we perform time-dependent (TD) vibrationally resolved phosphorescent rate and spectra calculations under different approximations, i.e., at the Frank-Condon (FC)[35] level and/or including Herzberg-Teller (HT)[36] effects, i.e., FC/HT. For these calculations, we tested the performance of different exchange correlation (xc) functionals for the optimization and hessian calculations of the involved triplet excited state. Based on the analysis of the results of the phosphorescent rate and spectra calculations under different approximations, we provide an appropriate computational recipe to perform these simulations in a computationally accurate and efficient way.[37–41]

2. COMPUTATIONAL DETAILS

2.1 Optimization and Frequency Calculations

All the ground state geometry optimizations and Hessian calculations were performed with density functional theory (DFT)[42–44] using the B3LYP[45–47] functional in combination with the 6-31G* basis set for all the atoms and the LANL2DZ[48] pseudopotential for Iridium. For the geometry optimizations and hessian calculation of the first triplet excite state (T_1), unrestricted DFT (U-DFT) was used with the same functional and basis set as mentioned above for the ground state calculation (see discussion in the SI, Tables S2-S3). In addition, geometry optimizations of the higher-lying triplet excited states (T_1-T_4) were performed with time-dependent DFT (TD-DFT)[49–52] level of theory with the same functional and basis set as in the DFT calculations. The Gaussian 16 program package[53] was used for the optimization and for the Hessian calculations.

2.2 Phosphorescence Energy Calculations

Canonical CCSD(T) calculations were performed for the ad hoc system to evaluate the performance of DLPNO-CCSD(T). The latter method was used to evaluate the phosphorescence energies of **1-30**. The phosphorescence energies were obtained with the ΔSCF-DLPNO-CCSD(T) approach i.e., the energy difference between the singlet and triplet single point energy calculations at the optimized triplet minima. For the DLPNO-CCSD(T) calculations, tight Pair Natural Orbital (PNO) settings (TCutPairs = 10^{-5}, TCutPNO = 1×10^{-7}, TCutMKN = 10^{-3}) and very tight SCF settings (energy change 1×10^{-9} au) were used to reach reliable numerical accuracy. We also tested different reference determinants for the local coupled-cluster calculations. Specifically, for the ground-state calculations we tested restricted Hartree Fock (RHF) and restricted Kohn-Sham (RKS) determinants while for the triplet excited states we used unrestricted Hartree Fock (UHF), unrestricted Kohn-Sham (UKS), restricted open Hartree Fock (ROHF) and restricted open Kohn-Sham (ROKS) reference determinants.

The DLPNO-CCSD(T) calculations for complexes **1-30** were performed in combination with the def2-SVP basis set and def2-ECP pseudopotential for Iridium. For selected complexes we also performed full iterative DLPNO-CCSD(T_1) calculations to assess the recovery of correlation energy in the local method. All the DLPNO-CCSD(T) calculations were performed with Orca5.0 program package.[54]

Furthermore, DFT-based methods were used to calculate the phosphorescence energies. Specifically, both ΔSCF-DFT calculations along with the calculation of vertical emission energies with linear response TD-DFT were performed to estimate phosphorescence energies. The latter calculations were performed with different flavors of xc functionals, including pure functionals (N12[55], SOGGA11[56]), hybrid functionals (B3LYP, PBE0[57]), double-hybrid functional (B2PLYP[58], mPW2PLYP[59]), long-range-corrected functionals (CAM-B3LYP[60], LC-ωHPBE[61]), meta-hybrid

functional (MN15[62], M06HF[63], PW6B95[64]) and long-range corrected hybrid functional (ωB97X[65]). The use of the Tamm-Dancoff approximation (TDA)[66] within TD-DFT (i.e., TDA-DFT in the following), and which is known to give improved results for the triplet states, was also assessed.[67–69] The statistical error descriptors such as e.g., mean absolute deviation (MAD) and mean signed deviation (MSD) were calculated.

2.3 Characterization of the triplet excited states

In this work, we aim at quantitatively characterize the character of the electronically triplet excited states, especially those involved in the emission process. Towards this end, we have used the TheoDORE (Theoretical Density, Orbital Relaxation and Exciton analysis) package.[33] Due to interaction between the metal and the various ligands in Ir(III) complexes several types of excited state are possible, including metal-centred (MC), ligand-centred (LC), metal-to-ligand charge transfer (MLCT), ligand-to-metal charge transfer (LMCT) and ligand-to-ligand charge transfer (LLCT) states.[34] In TheoDORE, density matrices (DMs) are used to characterize the nature excited state of TMCs, and more specifically, the 1-electron transition DM (1TDM). The 1TDM provides a mapping between the initial (excited state) and the final (ground state) wavefunctions. The decomposition of the charge transfer number matrices into user-defined fragments (here corresponding to the metal atom and each of the N^N and C^N ligands) enables to quantify the contributions of the different excited state's types to the emissive triplet state. For these analyses, the 1TDM was obtained with TDA-CAM-B3LYP and TD-CAM-B3LYP (see discussion below).

2.4 Phosphorescent spectra and rates

The phosphorescence rates and spectra were performed in selected complexes of different characters (**4, 9, 15, 23, 24, 29**) at the the DFT, TD-DFT, and/or TDA-DFT levels of theory.[38,70] For these calculations the Adiabatic Hessian (AH) vibronic model and the FC approximation were

chosen, which have been proven to be appropriate to calculate the phosphorescent spectra of diverse molecular systems.[71–73] In addition, we have assessed for **29** the effect of including higher-order terms in the SOC expansion, that is the FC/HT approach, For all the rate calculations, lower frequencies up to 200 cm^{-1} were removed due to their anharmonic nature and their accompanying large displacement vectors. A Voigt-type function was used to simulate the lineshape of the spectra. Specifically, a gaussian and an inhomogeneous linewidth of 75 and 200 cm^{-1} were chosen, respectively.

The path integral approach relying on the harmonic oscillator approximation, as implemented in the Orca5.0 program package,[54] was used to compute the phosphorescent spectra and rates of the Ir(III) complexes. The B3LYP functional was used to calculate the Hessians at the optimized geometries of the ground and excited state. To account for scalar relativistic effects, we have used zero-order relativistic approximation (ZORA) Hamiltonian[74,75] with ZORA-DEF2-SVP basis set for all atoms except for Iridium, which made use of the SARC-ZORA-SVP basis set.[76] For the spin-orbit couplings (SOCs), we have used spin-orbit mean-field method with resolution of identity scheme (RI-SOMF) to accelerate the calculation of the coulomb integrals.[77] The adiabatic energies were calculated in the presence of solvent, with the Conductor-like Polarizable Continuum Model (CPCM)[78,79] to account for the solvation effects. Specifically, aiming at comparisons with available experimental data, DMSO was chosen for complexes **1**-**24**, **28** and **30**, whereas acetonitrile and dichloromethane (DCM) were used for complexes **25**-**27** and **29**; respectively. The adiabatic energy was computed with DLPNO-CCSD(T) with the same basis set and solvent model as discussed above. The adiabatic energy of the higher-lying T$_2$ state of complex 9 is based on the TDA-B3LYP results, as the possible variational collapse of the wavefunction with DLPNO-CCSD(T) prevent us from using the latter method for the higher-lying excited states.

3. RESULTS & DISCUSSION

For complexes **1**-**30** (see Table S2) extensive photophysical data is readily at hand. Specifically, the herein investigated complexes, except **29** has been the scope of an exhaustive photophysical characterization with the same setup and conditions.[18]

We start this section with the discussion of the results for the phosphorescence energies for the *ad hoc* model (see Figure 1b). Then, we assess the performance of DLPNO-CCSD(T) for the phosphorescence energies of complexes **1**-**30** against the experimental results and we assess the performance of different xc flavors against our theoretical best estimates, i.e., the DLPNO-CCSD(T) results. Next, we present the results of the excited state characterization by the transition density matrix and decomposition analysis. Lastly, we present the results of the phosphorescence spectra and rate calculations on selected iridium complexes characterized by different emissive scenarios.

3.1. Benchmarking the phosphorescence energy of the *ad hoc* model

The *ad hoc* model (**Figure 1b**) was used to assess the performance of DLPNO-CCSD(T) against canonical CCSD(T). Different basis sets and relativistic approaches were tested along the canonical CCSD(T) and DLPNO-CCSD(T) calculations. The results are shown in **Table 1**. Our best theoretical estimate for the phosphorescence energy is canonical CCSD(T) in combination with the def2-TZVP basis set and the def2-ECP pseudopotential for Iridium. It is important to mention that for the *ad hoc* model we have used CAM-B3LYP as initial guess for ΔSCF-DLPNO-CCSD(T) calculations. Using the latter basis sets, the ΔSCF-CCSD(T) calculations yield a phosphorescence energy of 1.46 eV. We note that no experimental values are available for the *ad hoc* model and therefore, we assessed the quality of the DLPNO-CCSD(T) calculations by tracing the amount of recovered electron correlation against the canonical CCSD(T) calculations. The

complete results can be found in Table S1. Larger errors are seen when perturbative triple excitations are used, i.e., DLPNO-CCSD(T), which recovers between the 87-91% of the total CCSD(T) energy, as compared to the full iterative triples approach, i.e. DLPNO-CCSD(T_1), which recovers between the 95-100% of the total CCSD(T) energy. However, looking at the total correlation energy recovery by DLPNO-CCSD(T) and DLPNO-CCSD(T_1), one can see that both methods succeed in recovering most of CCSD(T) correlation energy (see values between 99-101% in Table S1). Therefore, for the sake of computational ease, the cheaper DLPNO-CCSD(T) approach was chosen to calculate the phosphorescence energies of **1-30**.

Table 1: Computed Phosphorescence energy with different ΔSCF-DLPNO-CCSD(T) settings and with canonical ΔSCF-CCSD(T) for the *ad hoc* model (all values in eV).

Basis Set	DLPNO-CCSD(T) with ECP	DLPNO-CCSD(T) with ZORA	DLPNO-CCSD(T) with DKH	CCSD(T) with ECP
Def2-SV(P)	1.34	1.30	1.29	1.54
Def2-SVP	1.46	1.30	1.28	1.66
Def2-TZVP	1.24	1.23	1.22	1.46
Def2-QZVPP	1.31	1.25	1.24	-

To account for scalar relativistic effects different approaches were tested. Specifically, we used pseudopotentials but also ZORA (Zero-Order Relativistic approximation) and DKH (Douglas-Kross Hamiltonian)[80] Hamiltonians, which combined with the larger basis set i.e., def2-QZVPP, yield phosphorescence energies of 1.31, 1.25 and 1.24 eV, respectively (as shown in **Table 1**). Overall, and regardless of the relativistic approach used, there is no drastic change in the DLPNO-

CCSD(T) computed values. The effect of enlarging the basis set is more noticeable, with maximum deviations amounting up to 0.22 eV (see e.g., 1.46 eV and 1.24 eV in the first column of Table 1). The calculated phosphorescence energy with ΔSCF-DLPNO-CCSD(T) using ECP and the Def2-SVP basis set fully matches our theoretical best estimate (i.e., 1.46 eV). Although this coincidence is probably because of cancelation of errors, for the sake of computational ease, the latter protocol was chosen to calculate the phosphorescence energies of **1**-**30**.

3.2 Phosphorescence energies of complexes 1-30

After establishing a reliable ΔSCF-DLPNO-CCSD(T) protocol for the phosphorescence energies, we next turn into the discussion of the computed results for **1-30**. First, we focus on the effect of using different guesses for the DLPNO-CCSD(T) calculations. Recent studies on transition metal complexes showed that the use of a Kohn-Sham guess instead of a Hartree-Fock one often leads to more accurate results.[81–84] We thus, investigate these aspects for the phosphorescence energies of **1-30**. Specifically, orbital guesses from restricted Hartree-Fock (RHF), restricted open-shell Hartree-Fock (ROHF) and restricted Kohn-Sham (RCAM-B3LYP) were used for the ground state calculations while unrestricted Hartree-Fock (UHF), restricted open-shell Hartree-Fock (ROHF) and unrestricted Kohn-Sham (UCAM-B3LYP functional) were used for the triplet excited state calculations. The computed results are collected in Table S4 and S5 and graphically summarized in Figure 2. The use of a HF and/or ROHF orbital guess leads to overestimated phosphorescence energies with respect to the experimental values, complexes **1** and **5** behaving as outliers (see Table S4). This is also clearly seen in Figure 2. The use of a DFT guess for the DLPNO-CCSD(T) calculations leads to a narrower distribution of errors, which are additionally centered around the 0.0 value. Conversely, the use of a HF orbital guess for the DLPNO-CCSD(T) calculations leads to larger deviations, being the phosphorescence energies systematically overestimated.
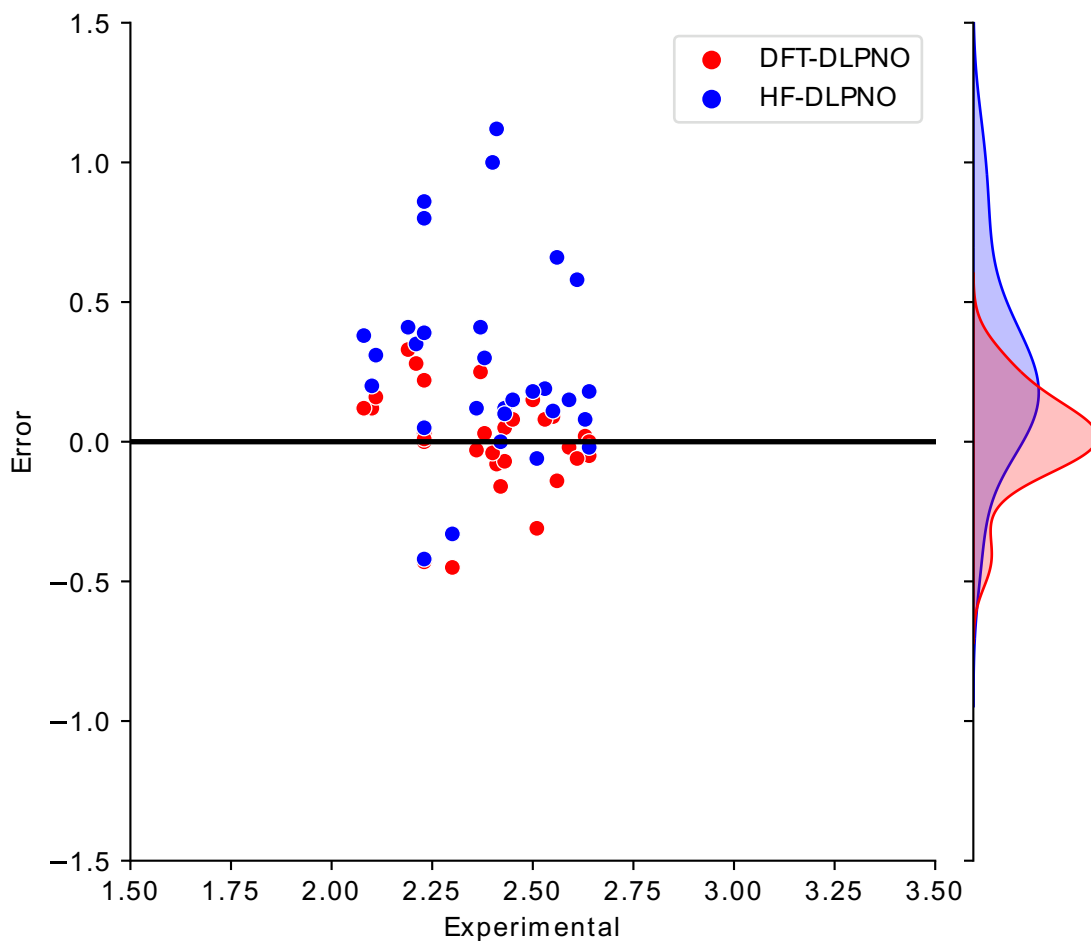
Figure 2: Errors (in eV) of the ΔSCF-DLPNO-CCSD(T) phosphorescence energy calculations when using different orbital guesses against the experimental values (in eV) of 1-30.

More in details, the MAD values amount up to 0.38 eV and 0.13 eV for HF-based and DFT-based approaches, respectively. These differences likely root on the different spin-density distributions obtained with the DFT-based and HF-based guesses for the excited state triplet calculations. Figure S2 shows exemplarily these differences for complexes **1**, **12** and **20**. The UHF plots are more

spread and show an enhancement of spin polarization as compared to the UKS ones. While the UHF solutions for the triplet excited states are highly spin-contaminated this is less of a problem for UKS (see values in Figure S2). This non-physical effect leads to an overestimation of the computed phosphorescence energies when using the UHF orbitals as a guess. All in all, in view of these results, the use of a UKS guess for the ΔSCF-DLPNO-CCSD(T) calculations is highly recommended and all the values discussed in the following make use of a UKS guess.

Next, we compared the effect of using full iterative triples (T_1) instead of the standard perturbative triples (T) for a few selected Ir(III) complexes. These results can be found in Table S4. The divergences between the two approaches is not very large (ca. 0.01-0.03 eV). Therefore, in view of the computed results and for the sake of computational ease, the use of the standard perturbative triples (T) seems to be more convenient. Further, we also compared the performance of ΔSCF-DLPNO-CCSD(T) for the different excited state types of **1**-**30**, which are preliminary assigned based on a qualitative analysis of their spin density distribution plots (see Tables S5 and S10). Note that a quantitative analysis of the character of the triplet excited state is presented in **Section 3.4.** These results are presented in **Figure S3**. ΔSCF-DLPNO-CCSD(T) performs more accurately for complexes with a triplet excited state of predominant LC character (see green points in **Figure S3**) than those with a predominant CT state (see pink points in **Figure S3**). MAD values of 0.06 and 0.19 eV, are obtained for ^{3}LC-based and ^{3}CT-based complexes, respectively. These observations are complementary to the ones obtained by Zysman-Colman et al. on similar complexes.[85–87] we have performed.

3.3. Assessing different DFT-based approaches against DLPNO-CCSD(T) for the phosphorescence energies

The ΔSCF-DLPNO-CCSD(T) values are used next to benchmarking several DFT-based approaches for the phosphorescence energies of **1**-**30**. We have employed three different approaches to calculate the phosphorescence energies, namely, i) ΔSCF-DFT ii) TDDFT and iii) TDA-TDDFT (see details in the Computational Details). Different flavors of xc functionals were assessed. The results are presented in **Figure 3**. Regardless of the choice of xc functional, the ΔSCF-DFT values (grey circles in **Figure 4**) are closer to the ΔSCF-DLPNO-CCSD(T) reference values followed by TDA-TDDFT (red triangles) and TDDFT values (blue stars). Exemplarily for CAM-B3LYP, the MAD values for the ΔSCF-CAM-B3LYP, TDA-CAM-B3LYP and TD-CAM-B3LYP approaches are 0.14, 0.25 and 0.40 eV, respectively. This trend is conserved regardless of the chosen xc functional. These results are consistent to those obtained by some of us for Pt(II) complexes.[24] Comparing TDDFT and TDA-TDDFT, the later one is more accurate, especially in combination long-range-separated functional (see e.g., CAM-B3LYP and LC-HPBE in **Figure 3**). In the latter cases, the MAD values for TDDFT is almost twice as large as the one obtained with TDA-TDDFT. Also, in case of long-range-separated functionals, TDDFT underestimates the phosphorescence energies while TDA-TDDFT overestimates them. For instance, the MSD for LC-HPBE is 0.60 and -0.22 eV for TDDFT and TDA-TDDFT, respectively (see Table S8). However, in the case of pure functionals (N12 and SOGGA11) or hybrid functionals (B3LYP and PBE0), the effect of choosing TDDFT and TDA-TDDFT is less significant, as both approached render similar MAD and MSD values.

Let us discuss a bit more in detail the ΔSCF-DFT results. **Figure 4** collects the results for the different xc functionals. Overall, hybrid functionals are more accurate than pure functional (see

also Table S9), with acceptable MAD values (< 0.3 eV) for the former xc functionals. In the case of double hybrid functional (B2PLYP and mPW2PLYP), a MAD value of 0.27 eV is obtained for both functionals. Among the meta-hybrid functionals (MN15, PW6B95 and M06HF), MN15 is the best performing functional with a MAD of 0.16 eV. Conversely, M06HF is the worst performing functional (MAD of 0.94 eV).
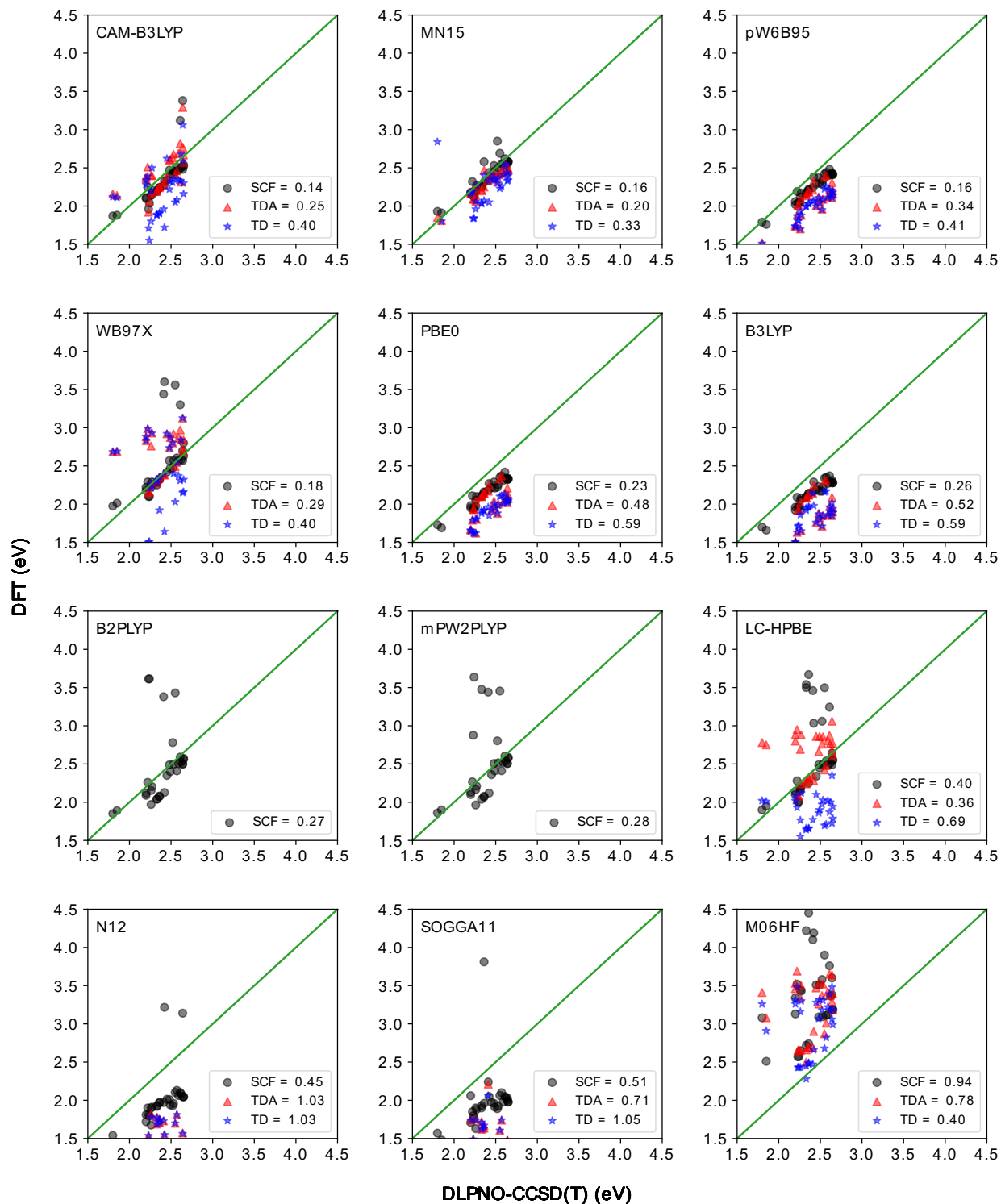
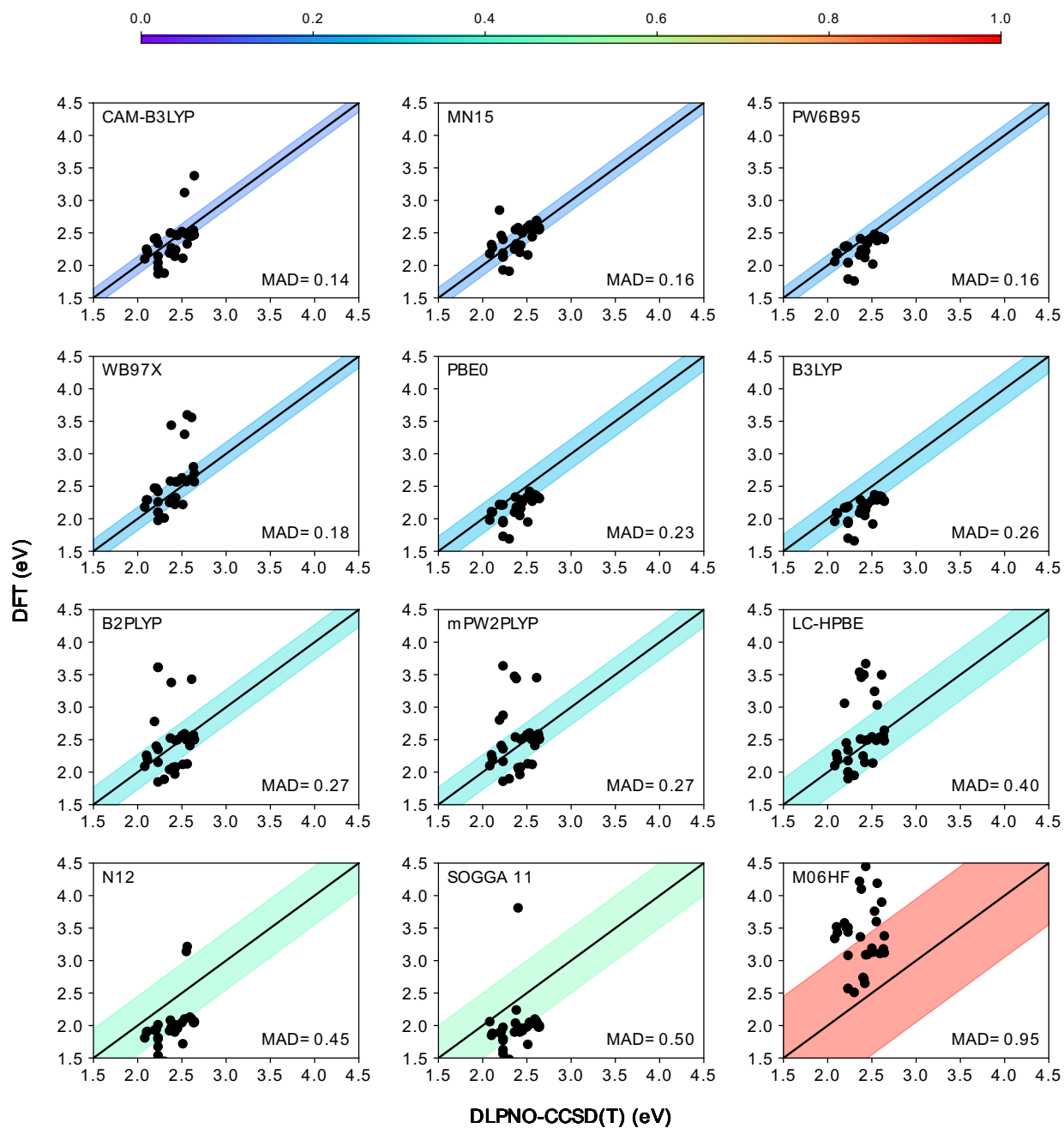**Figure 3:** Comparing different DFT protocols to DLPNO-CCSD(T) values.

17

Figure 4: Comparison of ΔSCF-DFT approach to DLPNO-CCSD(T) values.

3.4 Excited state character of T_1

The excited state character of the emitting state in heteroleptic Ir(III) complexes can be finely tuned by the choice of cyclometalating (C^N) and ancillary (N^N) ligands. Often, a certain degree of admixture between different excited states is found.[88,89] For instance, the T_1 character of the archetypal Ir(III) [Ir(ppy)$_2$(bpy)]$^+$ complex (**29**) is known to be of mixed ^{3}MLCT/^{3}LLCT/^{3}LC character. By ligand substitutions and/or by combining different C^N and N^N ligands we can easily tune the character of the emitting state. For instance, phosphorescence spectral band shape analyses shows that broad and structureless emission is described for ^{3}CT-based states whereas highly structured emission is described for ^{3}LC-based states.[90,91] Also, and because of the likely presence of close-lying triplet excited states of different character, the phosphorescence properties are often heavily affected by the chemical surroundings (e.g., solvent, counterions, concentration and crystal packing effects or host medium in the emissive layer of an OLED device).[88,92,93] Thus, not only the position of the emission band and its intensity might be modulated by the environment but even a solvent-driven switch of the character of T_1 has been reported for several heteroleptic Ir(III) complexes.[94]

DiLuzio et al.[18], previously classified the emissive scenario and character of T_1 based on a qualitative analysis of the emission spectra. Here, and based on our analyses, we provide a more quantitative characterization of the lowest excited triplet state T_1. From a computational viewpoint, the characterization of the excited states can easily be done by e.g., the visual inspection of the electronic energies, electron density difference or spin density distribution plots and/or by electronic population analyses such as, natural population analysis (NPA), natural bond orbitals (NBOs) and natural transition orbitals (NTOs).[95] However, quantitative approaches enabling to e.g., quantify the degree of admixture between different excited states contributing to T_1 are

necessary to unambiguously characterize the character of T_1. The transition density matrix and decomposition analysis of the TD-DFT results, as implemented in THEODORE, has been successfully applied to characterize the excited states of both organic[96,97] and inorganic[98] molecular systems. We performed the decomposition analysis of the T_1 excited state for **1-30**. **Figure 5** collects the TDA-CAM-B3LYP results while the results obtained with TD-CAM-B3LYP are presented in Figure S4. We note remarkable different results between the two approaches. As mentioned above, TDA-DFT renders improved results for the phosphorescence energies as compared to TD-DFT. Likewise, we are confident that the analysis of the character of T_1 based on the TDA-CAM-B3LYP results is more reliable than the one obtained with TD-CAM-B3LYP. Indeed, the concomitant analysis of the computed TDA-DFT spectra and their best correspondence with the experimental findings (see e.g., the results for spectra analysis in section 3.5) further support the overall better performance of TDA-DFT vs TD-DFT. As seen in **Figure 5**, most of the complexes possess a predominant ^{3}LLCT character or a predominant ^{3}LC character. For instance, **4** has a contribution of 25%, 34% and 39% of LC, MLCT and LLCT character, respectively. Therefore, **4** can be regarded to be of predominant ^{3}CT character. As expected, none of the investigated complexes possess significant ^{3}MC and ^{3}LMCT character. All the complexes except **3, 4, 12, 17, 25, 26** and **28** possess a significant ^{3}MLCT character, which ranges from 30% for **3, 25** and **26** up to 35% for **17**. The amount of ^{3}MLCT character of T_1 typically correlates with the zero-field-splitting value and with the radiative lifetimes (Table S7 collects the computed and experimental radiative rates for selected complexes). Thus, an enhanced ^{3}MLCT character of T_1 typically leads to shorter excited state lifetimes, which are beneficial for e.g., OLEDs applications (see discussion below in Section 3.5).[89]
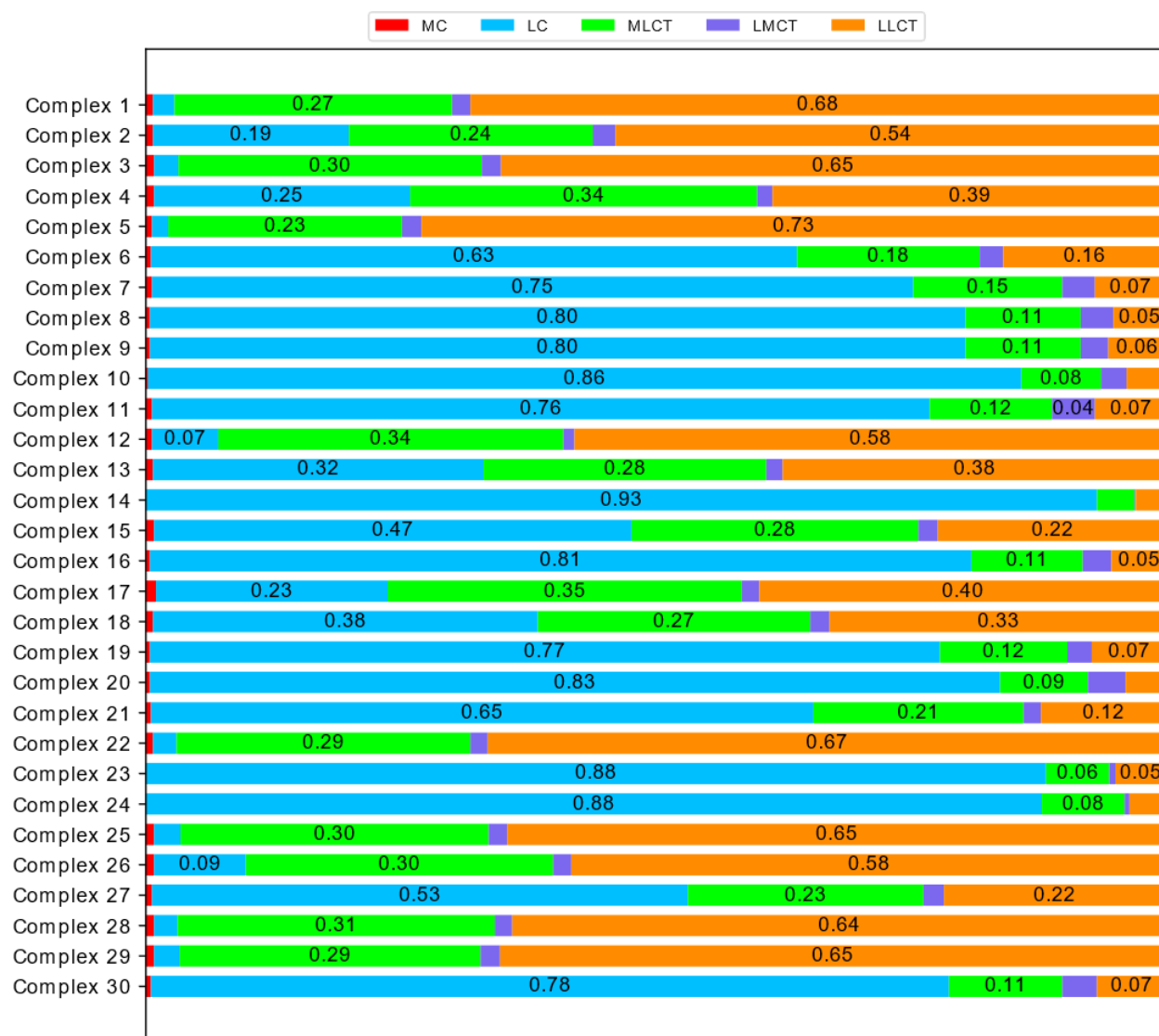
Figure 5: Fragment decomposition analysis of T_1 of **1**-**30** with TDA-CAM-B3LYP.

3.5. Phosphorescence spectra and rates calculations

Phosphorescence spectra and rate calculations were performed for selected complexes. A focus was set on assessing the calculations of these properties for three different scenarios, that are: (i) complexes emitting from a predominant local ^{3}LC T_1 state, (ii) complexes emitting from a predominant CT-based T_1 state (typically the mixed ^{3}MLCT/^{3}LLCT case); and (iii) complexes possessing close-lying triplet excited states, so that a thermal equilibrium between low-lying triplet

excited states is possible. Needless to say, intermediate regimes between scenarios (i) and (ii) are also possible, see discussion below for **4** and **15**. Finally, possible complexes belonging to case (iii) where detected by performing TDA-DFT optimizations of the higher-lying excited states. The results are presented in Table S6. If the adiabatic energy difference between T_1 and a higher-lying T_n state is < 0.05 eV, those can likely be thermally populated from T_1 and contribute to the phosphorescence observed experimentally. This latter emissive scenario is also found for some Pt(II) complexes, as some of us have reported previously.[24] Within the series of studied complexes, and in view of the computed energy differences, **9** and **10**, are likely case (iii) complexes. This situation is not uncommon for other $[Ir(C\wedge N)^2(N\wedge N)]^+$ complexes, see e.g. Refs. 99 and 100.

First, we analyze the effect of including or not HT effects on the computed rates and spectra. Complex **29** was chosen for such a purpose. Note that **29** is a case (ii) complex. The S_0 and T_1 geometries along with the Hessian calculations were performed with B3LYP and UB3LYP, respectively (see the computed phosphorescence spectra with this protocol in the top panels in Figure 6). For assessment purposes, we also show the calculated spectra using TD-B3LYP and TDA-B3LYP for T_1 (see middle and bottom panels, respectively, in Figure 6). Regardless of the level used, the FCHT and FC approaches deliver very similar phosphorescence spectra. Being these complexes characterized by sizable SOCs values between S_0 and T_1 this is not surprising. The inclusion of HT effects leads to more vibronically-resolved spectra, which arise on the contribution of the extra HT terms, but the overall effect on the spectrum shape is not significant. Under these circumstances, the cheaper FC approach was used to calculate the phosphorescence spectra and rates for the rest of complexes. As can be seen in the Figure 6, we have used three DFT-based approaches to compute spectra i.e., UDFT, TD-DFT and TDA-DFT. The displacement

vector (K*K) is lowest for the TDA-DFT approach. This means that the changes in the ground and excited state geometries are less significant with the latter approach and guarantees in a larger extent the validity of the harmonic approximation for these calculations. Therefore, for the rest of complexes we have used TDA-DFT to simulate their rates and spectra.

We note that **29** possesses a mixed ³MLCT/³LLCT character. Cyclometalated Ir(III) complexes with significant ³CT character, such as e.g., **29**, typically yield emission bands without fine structure.[94] This is reflected in the calculated phosphorescence spectrum of **29**, which shows a single very predominant vibronic contribution to its spectrum. We note, however, that the broadening is not fully matched by our calculations as other important sources of broadening (e.g., environment-induced inhomogeneous broadening) and which may become especially relevant for emissive states of significant ³CT character, such as e.g., **29**, are not explicitly considered in our calculations. In **Table 2,** we compare the computed radiative rates with the experimental one. A quantitative agreement between the computed and experimental pieces of evidence is found, specially with the TDA-B3LYP approach, which o23utperforms the other two DFT-based approaches. These results are aligned with the results obtained for the spectra and displacement vectors (see **Figure 6**).
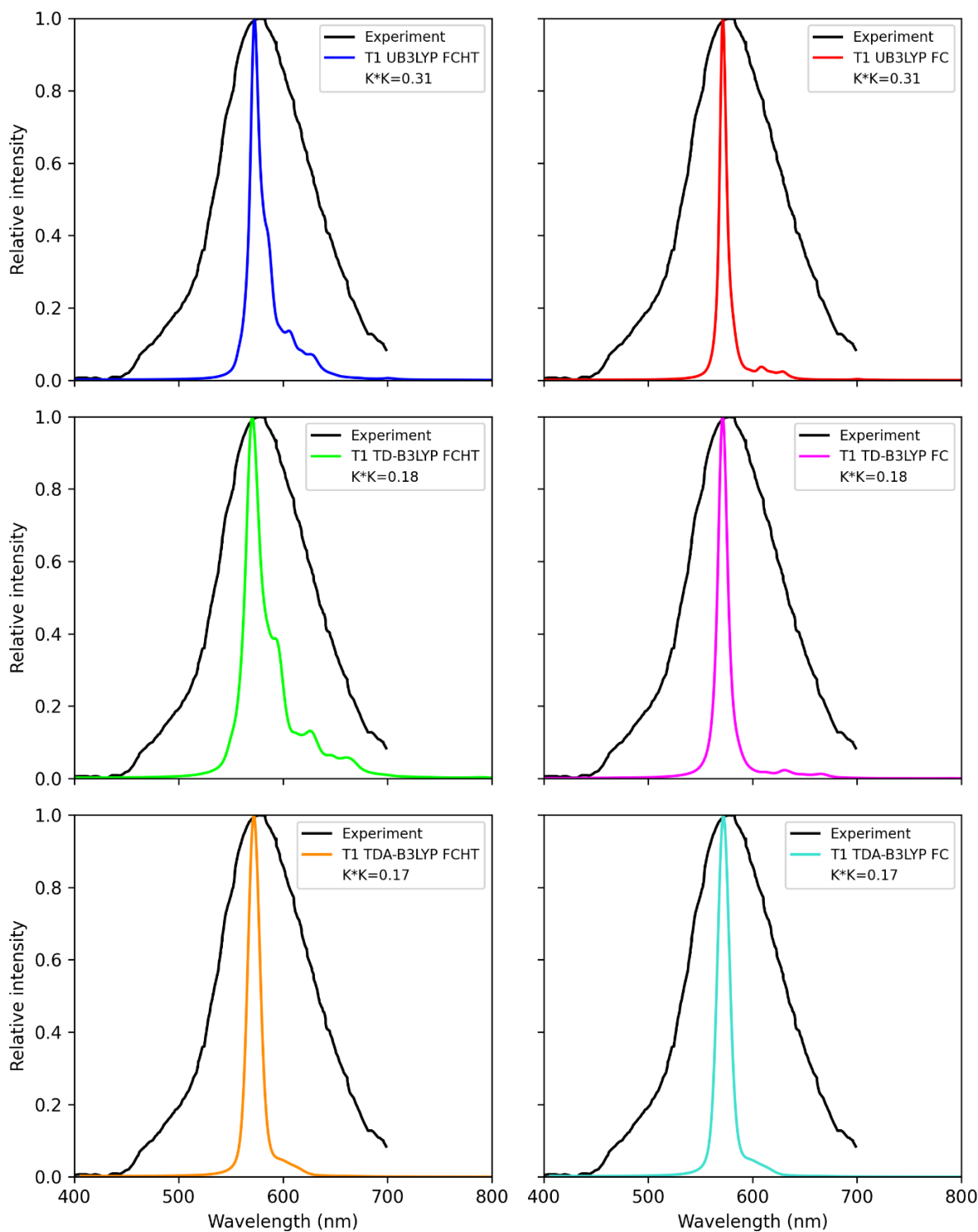
Figure 6: Comparison of different approaches to get the phosphorescent spectra of complex 29, experimental spectra (black line) was taken from Ref. 94 and the solvent used was CH_2Cl_2 (DCM).

24

Table 2: Computed and experimental radiative rates of Complex **29**.

Theoretical approach	Theo. radiative rate (s-1)	Exp. radiative rate (s-1)
TDA-B3LYP without HT	3.0×10^5	3.5×10^5
U-B3LYP without HT	2.0×10^5	
TD-B3LYP without HT	8.8×10^5	

Table S7 collects the computed phosphorescence rate values for selected complexes (i.e., **4**, **9**, **15**, **23**, **24** and **29**) with TDA-B3LYP. TDA-B3LYP was chosen here in view of the smaller displacement factors obtained with this level of theory (see discussion above for **29**) but also because we here aim to study the phosphorescence properties from higher-lying excited states, i.e., T_n, which are energetically close to T_1, and thus, making unfeasible the use of UB3LYP. Further, we also tested two xc functionals, i.e., B3LYP and CAM-B3LYP, to simulate the spectra. A comparison of the computed spectra, rates and displacement vectors for selected compounds is shown in Table S7, S11 and Figure S7. As seen in Table S11 and Figure S7, TDA-B3LYP outperforms TDA-CAM-B3LYP, both in view of the better recovery of the experimental spectrum's shape but also in view of the smaller computed displacement factors with the former approach. The computed phosphorescence spectra of **23**-**24**; **4**, **15**; and **9**, with TDA-B3LYP are shown in Figures 7, 8 and 9; respectively.

Let us start the discussion with the complexes emitting from a predominant ^{3}LC T_1 state, i.e., **23** and **24**. The LC character of **23** and **24** amounts up to 88%, see Figure 5. The electron density difference plots of their T_1 states are shown for completeness in Figure 7, which clearly highlights the involvement of the cyclometalated C^N ligand for T_1. Conversely to **29**, who possesses a predominant CT character, the phosphorescence spectra of **23** and **24** are vibronically-resolved

(see Figure 7). The agreement between the experimental and computed spectra is excellent, both in the position and relative intensities of the vibronic bands. Note that the computed spectra were shifted for comparative purposes (see dashed line in Figure 7). We note that, in contrast to **29**, the experimental broadening is also recovered by our calculations. Thus, for complexes with a predominant ^{3}LC T_1 state, the vibronic progression is mostly responsible for the experimental broadening. Accordingly, and not surprisingly because of the local excitation character of their T_1, these complexes should be less affected by the environment-induced inhomogeneous broadening.
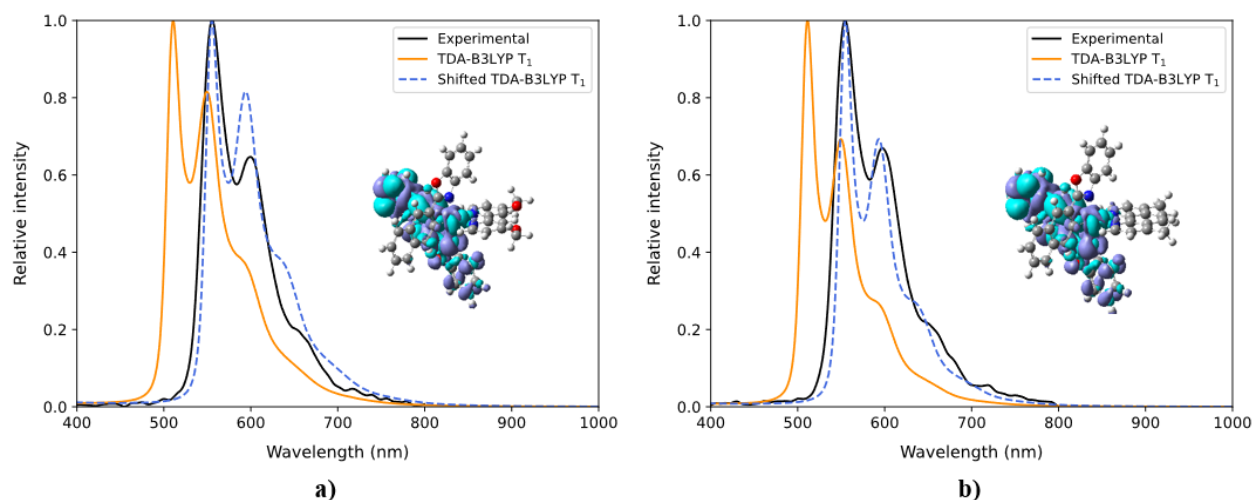

Figure 7: Computed phosphorescent spectra and electron density difference plot of complexes emitting from a predominant ^{3}LC T_1 state, i.e., complex 23 (**a**) and complex 24 (**b**), The solvent used was DMSO and the experimental data is taken from Ref. 18. The cyan and violet color in the electron density difference plot shows decrease in the electron density and increase in the electron density, respectively, during the electron transition.

Let us move the discussion to complexes **4** and **15**. Complexes **4** and **15** possess a larger amount of CT character (ca. 73% and 50%; respectively see Figure 5) than **23** and **24** but a lesser

percentage than **29** (ca. 94%). Complexes **4** and **15** correspond, thus, to an intermediate regime between the predominant LC and CT cases. While the T_1 state of **4** can be better categorized as a predominant mixed ^{3}MLCT/^{3}LLCT state, the non-negligible ^{3}LC character of the T_1 of **15** leads to a mixed ^{3}MLCT/^{3}LLCT/^{3}LC state. However, the subtle difference on their T_1 character cannot be scrutinized through a simple visual inspection of their T_1 electron density difference plots (see Figure 8). Analogously to **29**, the computed phosphorescence spectra of **4** and **15** are not vibronically resolved because of the significant CT character of their T_1 state. The computed spectra are in good agreement with their experimental counterparts, especially in their overall shape. However, obtaining the correct broadening for these complexes remains difficult (see discussion above for **29**). In comparison to **29**, the non-negligible LC-contribution for **4** and **15** leads to broader emission profiles. Specifically, the computed broadening of **4** is overestimated with respect to the experimental one (see Figure 8a). Conversely, the computed broadening for **15** is well matched with respect to the experimental one (see Figure 8b), but this is likely to occur incidentally in this case.
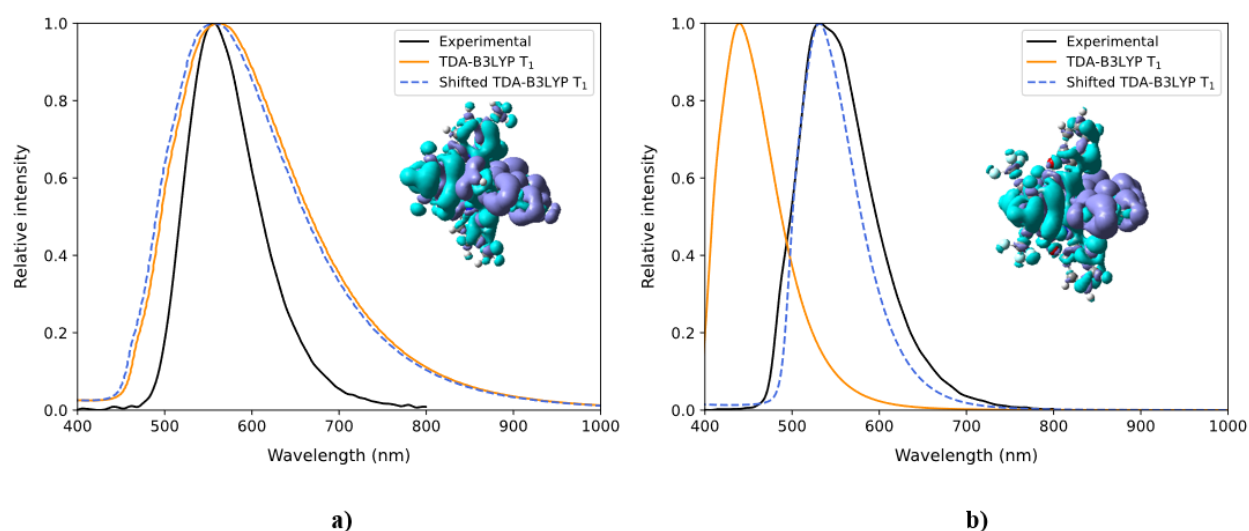

a)   b)

Figure 8: Computed Phosphorescent spectra and electron density difference of charge transfer Ir(III) complexes **a)** complex 4 and **b)** complex 15. The solvent used was DMSO and the experimental data is taken from Ref. 18. The cyan and violet color in the electron density difference plot shows decrease in the electron density and increase in the electron density, respectively, during the electron transition.

We turn the discussion into complexes possessing close-lying triplet excited states, so that a thermal equilibrium between low-lying excited states is likely at room temperature. As mentioned above, 9 belongs to the latter emitting scenario (i.e., case (iii)). For 9, the computed adiabatic energy gap between T_1 and its closest lying triplet state, i.e., T_2, is only 0.05 eV. (see Table S6). In view of the expected accuracy of TDA-B3LYP, one can assume that both states are close-lying, so that a thermal equilibrium between T_1 and T_2 is likely, and thus, both states may contribute to the emission spectrum. In order to prove this hypothesis, we computed the phosphorescence spectrum from T_1 and T_2 (see Figure 9). The electron density difference plots from T_1 and T_2 clearly show that they are different states. Specifically, while T_1 is mainly described as a predominant LC state (80%, see Figure 5), T_2 is mainly described as a mixed ^{3}MLCT/^{3}LLCT/^{3}LC state (see Table S12). However, none of their computed emission spectrum are in good agreement with the experimental one, neither in the position of the vibronic bands nor in their relative intensities, see Figures 9a-b. Next, we averaged the T_1 and T_2 spectra and we plotted it against the experimental one (see Figure 0c). In the latter case the agreement with the experimental counterpart is remarkable, both in the position of the vibronic bands and also in their relative intensities. These results along with the energetic ones unambiguously proof that a thermal equilibrium between T_1 and T_2 is likely at room temperature and that the two states concomitantly contribute to the phosphorescence spectrum of 9. We note that the exact percentage of T_1- and T_2-based emission

will predominantly be determined by the adiabatic energy gap between the states and their corresponding radiative rates.[101] In view of the difficulties to compute accurately these estimates we here used an arbitrary 50-50 percentage. We note that anomalous emission from T_2 cannot strictly be categorized as an anti-Kasha emission, because at its optimized geometry corresponds to the lowest triplet excited state.
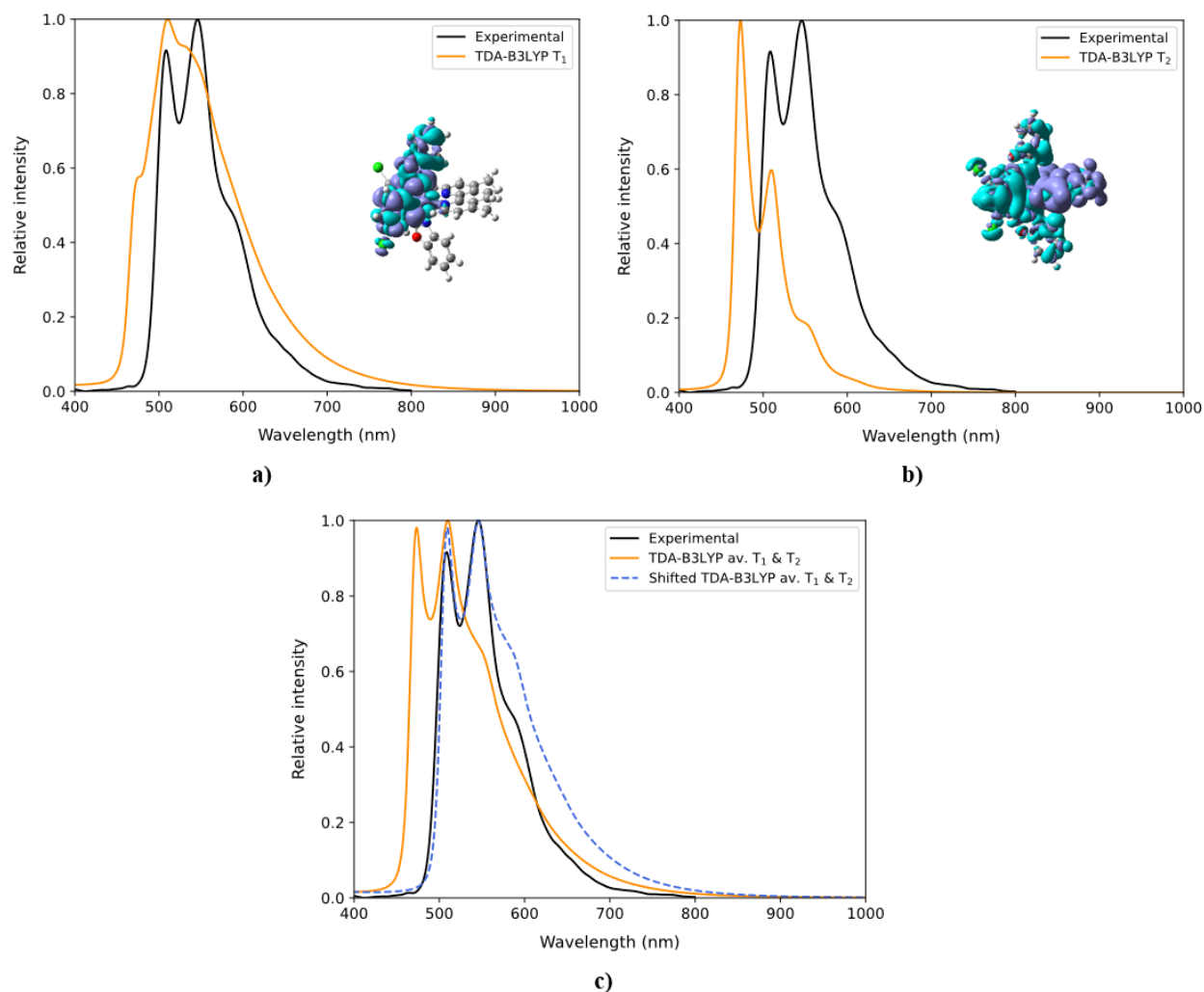

a)

b)

c)

Figure 9: Computed phosphorescent spectra and electron density difference of complex 9 with higher lying excited state **a)** spectra on first lowest excited triplet-state geometry **b)** spectra on second lowest excited triplet-state geometry **c)** spectra of average intensity from the two lowest close-lying triplet-state. The cyan and violet color in the electron density difference plot shows

decrease in the electron density and increase in the electron density, respectively, during the electron transition.

Finally, Table S7 collects the calculated phosphorescence rates with TDA-B3LYP for **4**, **9, 15**, **23**-**24** and **29**. The experimental global lifetimes are also tabulated in Table S7 for all the complexes (note that the purely radiative lifetime has been determined only for **29**). As mentioned above, the percentage of metal-character of T_1 typically correlates with the zero-field-splitting and with the radiative lifetimes. Overall, such a trend is also recovered by our calculations. Specifically, while the complexes emitting from a predominant ^{3}LC state (see e.g., **23**-**24**) possess rates on the order of 10^5, complexes possessing more ^{3}MLCT character (see e.g., **9**, **15**) generally yield phosphorescence rates on the order of 10^6. We also note that some complexes behave as outliers (see e.g., **29**) who despite its significant ^{3}MLCT character yields a phosphorescence rate on the order of 10^5 (however we note that both the computed and the experimentally determined rates match). Further investigations are needed to rationalize these discrepancies.

Conclusion

We have presented a comprehensive and exhaustive investigation on the calculation of the phosphorescence properties of a series of heteroleptic $[Ir(C\char94N)^2(N\char94N)]^+$ complexes. First, we assessed the performance of different flavors of DLPNO-CCSD(T) to calculate the phosphorescence energies of these complexes. For these calculations, the use of a Kohn-Sham guess instead of a Hartree-Fock one leads to more accurate phosphorescence energies and it is thus, highly recommended here. Based on our best theoretical DLPNO-CCSD(T) estimators we also explored the performance of different DFT-based approaches to calculate the phosphorescence energies. TDA-DFT and UDFT approaches are found to be superior to TD-DFT. Next, we performed transition density matrix and decomposition analysis of T_1 to characterize and classify different emissive scenarios. Finally, we also calculated the phosphorescence rates and spectra with the help of vibronic calculations. For both the characterization analyses and phosphorescence calculations we strongly recommend the use of TDA-DFT. A concomitant global analysis of the phosphorescence energies, excited state characters and phosphorescence rates and spectra, which is done for the first time here, enabled us to unambiguously classify the heteroleptic $[Ir(C\char94N)^2(N\char94N)]^+$ complexes according to their type of emissive scenario. Three clearly differentiated cases are found: (i) complexes emitting from a predominant local ^{3}LC T_1 state, (ii) complexes emitting from a predominant ^{3}CT-based T_1 state (typically the mixed ^{3}MLCT/^{3}LLCT case); and (iii) complexes possessing close-lying triplet excited states, so that a thermal equilibrium between low-lying triplet excited states and concomitant emission from several triplet states of different character, is likely. We note that intermediate situations between cases (i) and (ii) are also possible. Overall, this classification aligns well with the previous classification given in Ref. 18, but it additionally discloses the dual emissive scenarios, which are here disclosed thanks

to our holistic computational approach of combining the accurate calculation of phosphorescence energies, phosphorescence spectra and excited state characters. Thus, this study contributes to our previous reports disclosing complex emissive properties of transition metal complexes. From a computational viewpoint our study provides on the one hand side robust computational protocols to calculate the phosphorescence properties in heteroleptic $[Ir(C\char94 N)^2(N\char94 N)]^+$ and on the other hand side it highlights the complexity of their emissive processes and the need to go beyond the common believe in the community that the emissive properties of these complexes are solely determined by T_1.

NOTES

The authors declare no competing financial interest.

ORCID accounts

Prashant: https://orcid.org/0000-0002-0432-2790
Manuel: https://orcid.org/0000-0003-1463-7208
Davita: https://orcid.org/0000-0002-9447-4981

REFERENCES

1   H. Yersin, *Highly efficient OLEDs with phosphorescent materials*, John Wiley & Sons, 2008.

2   H. Yersin and J. Strasser, *Coord. Chem. Rev.*, 2000, **208**, 331–364.

3   E. Longhi and L. De Cola, *Iridium Optoelectron. photonics Appl.*, 2017, 205–274.

4   D. Jacquemin and D. Escudero, *Chem. Sci.*, 2017, **8**, 7844–7850.

5   D. Escudero, *Chem. Sci.*, 2016, **7**, 1262–1267.

6   D. Escudero, in *Transition Metals in Coordination Environments*, Springer, 2019, pp. 259–287.

7   D. Escudero, *ChemPhotoChem*, 2019, **3**, 697–701.

8   K. K.-W. Lo, M.-W. Louie and K. Y. Zhang, *Coord. Chem. Rev.*, 2010, **254**, 2603–2622.

9   G. Boverman, X. Shi, V. E. Cotero, R. J. Filkins, A. M. Srivastava, P. W. Lorraine, V. B. Neculaes and A. N. Ishaque, in *Clinical and Translational Neurophotonics; Neural Imaging and Sensing; and Optogenetics and Optical Manipulation*, International Society for Optics and Photonics, 2016, vol. 9690, p. 969018.

10   D. N. Tritton, F.-K. Tang, G. B. Bodedla, F.-W. Lee, C.-S. Kwan, K. C.-F. Leung, X. Zhu and W.-Y. Wong, *Coord. Chem. Rev.*, 2022, **459**, 214390.

11   T. M. Monos and C. R. J. Stephenson, *Iridium Optoelectron. Photonics Appl.*, 2017, 541–581.

12   D. Tordera, M. Delgado, E. Orti, H. J. Bolink, J. Frey, M. K. Nazeeruddin and E. Baranoff, *Chem. Mater.*, 2012, **24**, 1896–1903.

13   Q. Pei, G. Yu, C. Zhang, Y. Yang and A. J. Heeger, *Science (80-.)*., 1995, **269**, 1086–1088.

14   M. Yu, Q. Zhao, L. Shi, F. Li, Z. Zhou, H. Yang, T. Yi and C. Huang, *Chem. Commun.*, 2008, 2115–2117.

15   L. Zhang and D. Ding, *View*, 2021, **2**, 20200179.

16   H. Huang, S. Banerjee and P. J. Sadler, *ChemBioChem*, 2018, **19**, 1574–1589.

17   F. Legalite, D. Escudero, Y. Pellegrin, E. Blart, D. Jacquemin and O. Fabrice, *Dye. Pigment.*, 2019, **171**, 107693.

18   S. DiLuzio, V. Mdluli, T. U. Connell, J. Lewis, V. VanBenschoten and S. Bernhard, *J. Am. Chem. Soc.*, 2021, **143**, 1179–1194.

19   I. Soriano-Díaz, E. Ortí and A. Giussani, *Inorg. Chem.*, 2021, **60**, 13222–13232.

20   X. Zhang, D. Jacquemin, Q. Peng, Z. Shuai and D. Escudero, *J. Phys. Chem. C*, 2018, **122**, 6340–6347.

21   K. Y. Zhang, P. Gao, G. Sun, T. Zhang, X. Li, S. Liu, Q. Zhao, K. K.-W. Lo and W. Huang, *J. Am. Chem. Soc.*, 2018, **140**, 7827–7834.

22   Y. Yeh, Y. Cheng, P. Chou, G. Lee, C. Yang, Y. Chi, C. Shu and C. Wang, *ChemPhysChem*, 2006, **7**, 2294–2297.

23   S. Kumar, Y. Hisamatsu, Y. Tamaki, O. Ishitani and S. Aoki, *Inorg. Chem.*, 2016, **55**, 3829–3843.

24   P. Kumar and D. Escudero, *Inorg. Chem.*, 2021, **60**, 17230–17240.

25   G. Baryshnikov, B. Minaev and H. Ågren, *Chem. Rev.*, 2017, **117**, 6500–6537.

26   J. Guo, X. Pan, J. Li, W. Wu and J. Zhang, *Spectrochim. Acta Part A Mol. Biomol. Spectrosc.*, 2019, **216**, 179–189.

27   M. Kleinschmidt, C. van Wüllen and C. M. Marian, *J. Chem. Phys.*, 2015, **142**, 94301.

28   R. J. Bartlett, in *Theory and Applications of Computational Chemistry*, Elsevier, 2005, pp.

1191–1221.

29   C. Riplinger and F. Neese, *J. Chem. Phys.*, 2013, **138**, 34106.

30   C. Riplinger, B. Sandhoefer, A. Hansen and F. Neese, *J. Chem. Phys.*, 2013, **139**, 134101.

31   M. Saitow, U. Becker, C. Riplinger, E. F. Valeev and F. Neese, *J. Chem. Phys.*, 2017, **146**, 164105.

32   Y. Guo, C. Riplinger, U. Becker, D. G. Liakos, Y. Minenkov, L. Cavallo and F. Neese, *J. Chem. Phys.*, 2018, **148**, 11101.

33   F. Plasser, *J. Chem. Phys.*, 2020, **152**, 84108.

34   S. Mai, F. Plasser, J. Dorn, M. Fumanal, C. Daniel and L. González, *Coord. Chem. Rev.*, 2018, **361**, 74–97.

35   E. U. Condon, *Phys. Rev.*, 1928, **32**, 858.

36   G. Herzberg and E. Teller, *Zeitschrift für Phys. Chemie*, 1933, **21**, 410–446.

37   K. Mori, T. P. M. Goumans, E. Van Lenthe and F. Wang, *Phys. Chem. Chem. Phys.*, 2014, **16**, 14523–14530.

38   R. Grotjahn and M. Kaupp, *J. Phys. Chem. A*, 2021, **125**, 7099–7110.

39   A. Baiardi, J. Bloino and V. Barone, *J. Chem. Theory Comput.*, 2013, **9**, 4097–4115.

40   P. P. Roy, S. Kundu, N. Makri and G. R. Fleming, *J. Phys. Chem. Lett.*, 2022, **13**, 7413–7419.

41   S. Kundu, P. P. Roy, G. R. Fleming and N. Makri, *J. Phys. Chem. B*, 2022, **126**, 2899–2911.

42   P. Hohenberg, *Phys. Rev*, 1965, **140**, A1133–A1138.

43   R. G. Parr, *Oxford Univ. Press*, 1989, **1**, 989.

44   W. Kohn and L. J. Sham, *Phys. Rev.*, 1965, **140**, A1133.

45   C. Lee, W. Yang and R. G. Parr, *Phys. Rev. B*, 1988, **37**, 785.

46   A. D. Becke, *J. Chem. Phys.*, 1992, **96**, 2155–2160.

47   A. D. Becke, *J. Chem. Phys*, 1993, **98**, 5648–5652.

48   P. J. Hay and W. R. Wadt, *J. Chem. Phys.*, 1985, **82**, 270–283.

49   E. Runge and E. K. U. Gross, *Phys. Rev. Lett.*, 1984, **52**, 997.

50   M. E. Casida, in *Recent Advances In Density Functional Methods: (Part I)*, World Scientific, 1995, pp. 155–192.

51   E. K. U. Gross, J. F. Dobson and M. Petersilka, *Density Funct. theory II*, 1996, 81–172.

52   M. A. L. Marques and E. K. U. Gross, in *A Primer in Density Functional Theory*, Springer, 2003, pp. 144–184.

53   M. J. Frisch, G. W. Trucks, H. B. Schlegel, G. E. Scuseria, M. A. Robb, J. R. Cheeseman, G. Scalmani, V. Barone, G. A. Petersson and H. Nakatsuji, *Wallingford CT*.

54   F. Neese, 2012.

55   R. Peverati and D. G. Truhlar, *J. Chem. Theory Comput.*, 2012, **8**, 2310–2319.

56   R. Peverati, Y. Zhao and D. G. Truhlar, *J. Phys. Chem. Lett.*, 2011, **2**, 1991–1997.

57   J. P. Perdew, M. Ernzerhof and K. Burke, *J. Chem. Phys.*, 1996, **105**, 9982–9985.

58   S. Grimme, *J. Chem. Phys.*, 2006, **124**, 34108.

59   T. Schwabe and S. Grimme, *Phys. Chem. Chem. Phys.*, 2006, **8**, 4398–4401.

60   T. Yanai, D. P. Tew and N. C. Handy, *Chem. Phys. Lett.*, 2004, **393**, 51–57.

61   T. M. Henderson, A. F. Izmaylov, G. Scalmani and G. E. Scuseria, *J. Chem. Phys.*, 2009, **131**, 44108.

62   S. Y. Haoyu, X. He, S. L. Li and D. G. Truhlar, *Chem. Sci.*, 2016, **7**, 5032–5051.

63   Y. Zhao and D. G. Truhlar, *J. Phys. Chem. A*, 2006, **110**, 13126–13130.

64   Y. Zhao and D. G. Truhlar, *J. Phys. Chem. A*, 2005, **109**, 5656–5667.

65   J.-D. Chai and M. Head-Gordon, *J. Chem. Phys.*, 2008, **128**, 84106.

66   S. Hirata and M. Head-Gordon, *Chem. Phys. Lett.*, 1999, **314**, 291–299.

67   M. J. G. Peach, N. Warner and D. J. Tozer, *Mol. Phys.*, 2013, **111**, 1271–1274.

68   M. J. G. Peach, M. J. Williamson and D. J. Tozer, *J. Chem. Theory Comput.*, 2011, **7**, 3578–3585.

69   Y. Wang and G. Wu, *Int. J. Quantum Chem.*, 2008, **108**, 430–439.

70   R. Schira and C. Latouche, *Dalt. Trans.*, 2021, **50**, 746–753.

71   A. Stoliaroff, J. Rio and C. Latouche, *New J. Chem.*, 2019, **43**, 11903–11911.

72   F. Massuyeau, E. Faulques and C. Latouche, *J. Chem. Theory Comput.*, 2017, **13**, 1748–1755.

73   B. de Souza, G. Farias, F. Neese and R. Izsak, *J. Chem. Theory Comput.*, 2019, **15**, 1896–1904.

74   E. van Lenthe, E.-J. Baerends and J. G. Snijders, *J. Chem. Phys.*, 1993, **99**, 4597–4610.

75   C. van Wüllen, *J. Chem. Phys.*, 1998, **109**, 392–399.

76   J. D. Rolfes, F. Neese and D. A. Pantazis, *J. Comput. Chem.*, 2020, **41**, 1842–1849.

77   F. Neese, *J. Chem. Phys.*, 2005, **122**, 34107.

78   A. Klamt and G. Schüürmann, *J. Chem. Soc. Perkin Trans. 2*, 1993, 799–805.

79   D. M. York and M. Karplus, *J. Phys. Chem. A*, 1999, **103**, 11060–11079.

80   M. Reiher, *Theor. Chem. Acc.*, 2006, **116**, 241–252.

81   F. Neese, T. Schwabe, S. Kossmann, B. Schirmer and S. Grimme, *J. Chem. Theory Comput.*, 2009, **5**, 3060–3073.

82   M.-P. Kitsaras and S. Stopkowicz, *J. Chem. Phys.*, 2021, **154**, 131101.

83   C. J. Schattenberg, T. M. Maier and M. Kaupp, *J. Chem. Theory Comput.*, 2018, **14**, 5653–

5672.

84   A. A. Chamkin and E. S. Serkova, *J. Comput. Chem.*, 2020, **41**, 2388–2397.

85   E. Zysman-Colman, *Iridium (III) in optoelectronic and photonics applications*, John Wiley & Sons, 2017.

86   S. Ladouceur and E. Zysman-Colman, *Eur. J. Inorg. Chem.*, 2013, **2013**, 2985–3007.

87   A. F. Henwood and E. Zysman-Colman, *Chem. Commun.*, 2017, **53**, 807–826.

88   D. Escudero and D. Jacquemin, *Dalt. Trans.*, 2015, **44**, 8346–8355.

89   H. Yersin, A. F. Rausch, R. Czerwieniec, T. Hofbeck and T. Fischer, *Coord. Chem. Rev.*, 2011, **255**, 2622–2652.

90   F. Monti, A. Baschieri, L. Sambri and N. Armaroli, *Acc. Chem. Res.*, 2021, **54**, 1492–1505.

91   K. P. S. Zanoni, B. K. Kariyazaki, A. Ito, M. K. Brennaman, T. J. Meyer and N. Y. Murakami Iha, *Inorg. Chem.*, 2014, **53**, 4089–4099.

92   M. Mauro, G. De Paoli, M. Otter, D. Donghi, G. D'Alfonso and L. De Cola, *Dalt. Trans.*, 2011, **40**, 12106–12116.

93   D. L. Rochester, S. Develay, S. Záliš and J. A. G. Williams, *Dalt. Trans.*, 2009, 1728–1741.

94   R. D. Costa, F. Monti, G. Accorsi, A. Barbieri, H. J. Bolink, E. Orti and N. Armaroli, *Inorg. Chem.*, 2011, **50**, 7229–7238.

95   M. Jaeger, L. Freitag and L. Gonzalez, *Coord. Chem. Rev.*, 2015, **304**, 146–165.

96   M. T. Do Casal, J. M. Toldo, F. Plasser and M. Barbatti, *Phys. Chem. Chem. Phys.*, 2022, **24**, 23279–23288.

97   M. T. do Casal, J. M. Toldo, M. Barbatti and F. Plasser, *Chem. Sci.*, 2023, **14**, 4012–4026.

98   P. A. Sánchez-Murcia, J. J. Nogueira, F. Plasser and L. González, *Chem. Sci.*, 2020, **11**, 7685–7693.

99 P. A. Scattergood, A. M. Ranieri, L. Charalambou, A. Comia, D. A. W. Ross, C. R. Rice, S. J. O. Hardman, J.-L. Heully, I. M. Dixon and M. Massi, *Inorg. Chem.*, 2020, **59**, 1785–1803.

100 L. Paul, S. Chakrabarti and K. Ruud, *J. Phys. Chem. Lett.*, 2017, **8**, 4893–4897.

101 D. Jacquemin and D. Escudero, *Phys. Chem. Chem. Phys.*, 2018, **20**, 11559–11563.